MODELING AND SIMULATION OF THE ANISOTROPIC THERMAL EXPANSION OF TI-6AL-4V PROCESSED BY PBF-LB/M

T. MAYER*, P. CAPOZZI*, M. HOFMANN*, F. FRISO**, R. RADIS**

**ZHAW Zurich University of Applied Sciences, Institute of Mechanical Systems, 8401, Winterthur, Switzerland*
***ZHAW Zurich University of Applied Sciences, Institute of Materials and Process Engineering, 8401, Winterthur, Switzerland*

DOI 10.3217/978-3-99161-089-2-019, license CC BY 4.0

ABSTRACT

Additive manufacturing (AM), particularly Laser Powder Bed Fusion of Metals (PBF-LB/M), enables the production of geometrically complex Ti-6Al-4V components with high precision and design flexibility for a wide range of applications in the aerospace, chemical and process engineering, energy, and biomedical sectors. However, rapid solidification in PBF-LB/M produces a non-equilibrium martensitic α' microstructure with pronounced texture, leading to anisotropic mechanical and thermal behaviour. In particular, the apparent thermal expansion of PBF-LB/M Ti-6Al-4V has been found to be anisotropic due to strains induced during the $\alpha' \rightarrow \beta$ phase transformation (850–1000 °C). These transformation strains lead to pronounced apparent expansion along the build-direction and reduced in-plane apparent expansion. In PBF-LB/M manufactured components, this anisotropy can lead to unexpected residual stresses during the AM process or mechanical integrity issues during post-manufacturing heat-treatments or operation. This study focusses on the modelling of the anisotropic apparent expansion of Ti-6Al-4V and its implementation for Finite Element Analysis (FEA) to enable simulative investigations of the residual stress and distortion evolution in AM components.

A new model is introduced that separates isotropic thermal and transversally isotropic transformation strains. The model accounts for the path and temperature dependent transformation characteristics with varying transformation strains developing during heating ($\alpha' \rightarrow \beta$) and cooling ($\beta \rightarrow \alpha + \beta$). To make this model available to FEA, it was implemented in the FE software Abaqus via an UEXPAN subroutine. The effectiveness of the apparent expansion model and its implementation is demonstrated by comparing simulated and experimentally measured dilatometer curves. In addition, the impact of this anisotropic expansion on the residual stress development is investigated using thermo-mechanical process simulations of 1) a single laser welding track, and 2) the distortion of a cantilever following support structure removal.

The model successfully predicted the apparent expansion in a cylinder printed at a 45° angle. Furthermore, significant differences in vertical stress components and induced plastic strain in a single weld track were found. These are attributed to the additional constraints imposed by the transversally isotropic expansion underpinning the relevance of accounting for the transformation strain. Predictions of distortions in a cantilever following support removal were, however, significantly better when considering isotropic thermal strain only. This could potentially be explained by differences of the PBF-LB/M microstructure in the presence of a support structure. Understanding these mechanisms is crucial for optimizing the mechanical integrity and dimensional stability of PBF-LB/M-fabricated Ti-6Al-4V components in engineering applications subjected to post-processing heat-treatments or high-temperature applications.

Keywords: PBF-LB/M, Ti-6Al-4V, Thermal expansion, Anisotropy, Phase transformation

INTRODUCTION

The Laser Powder Bed Fusion process of Metals (PBF-LB/M) induces rapid solidification conditions with cooling rates exceeding 10^6 K/s [1-4]. In Ti-6Al-4V ,this results in a non-equilibrium martensitic α' microstructure within columnar prior β grains that grow epitaxially over multiple layers with their $\langle 001 \rangle_\beta$ direction oriented along the thermal gradient [5-13]. Acicular martensitic α' laths precipitate on the prior β grain boundaries obeying the Burgers orientation relationship [14-17] and growing along their invariant directions leading to a crystallographic and morphological texture due to crystallographic variant selection [10], [16]. Thus, the as-printed microstructure deviates significantly from the typically equiaxed bimodal $\alpha + \beta$ grain distribution observed in Ti-6Al-4V components conventionally manufactured by forging [18]. These anisotropic microstructural features [19-23], directly affect the mechanical response of PBF-LB/M-fabricated Ti-6Al-4V [9], [24].

While the anisotropy of the thermal expansion of Ti-alloys caused by the hexagonal close-packed crystal structure and the respective influence of alloy composition has been well studied [25-28], less attention has been paid to the effect of the particular PBF-LB/M microstructure and its impact to post-processing or service conditions. Recent experimental as well as theoretical studies of the present authors [29], have revealed that the apparent thermal expansion of PBF-LB/M-fabricated Ti-6Al-4V exhibits a pronounced build-direction dependence, particularly in the temperature range associated with the $\alpha' \rightarrow \beta$ transformation, i.e. 850 – 1000 °C. Vertically built specimens show a sharp increase in the apparent thermal expansion, whereas horizontally built ones exhibit a dip. These macroscopic effects are not fully captured by phase-specific lattice parameter measurements (e.g., synchrotron X-ray diffraction) [30], [31]. As outlined by [29], the build-direction dependent anisotropic apparent expansion can be explained by the crystallographic and morphological texture of the PBF-LB/M microstructure and the respective anisotropic transformation strains that are superimposed to the effectively isotropic thermal expansion. The anisotropic apparent expansion is expected to have an impact on additively manufactured (AM) components during post-processing heat-treatments or in service conditions at elevated temperatures.

Severe temperature gradients that occur during rapid transient melting and cooling processes together with phase transformations and local plastification during solidification cause either residual stresses or distortions in PBF-LB/M components [32]. To investigate the development of residual stresses and distortion during the PBF-LB/M process dedicated finite element (FE) based thermo-mechanical process simulation (TMPS) approaches have been developed [33-35]. Modern TMPS models are categorized into single-layer [36-44], and multi-layer TMPS models [45-50].

Single-layer models are focused on the laser beam vicinity, while multi-layer approaches are used to investigate temperature, stress, and distortion fields in PBF-LB/M structures. To study temperatures and stresses along the laser trajectory, single-layer TMPS models typically use a moving Goldak heat source [51] to simplify the complex melt-pool physics [38]. Such models have been used to study the effect of process parameters on microstructure [42-44], distortion [52], and residual stress [35], [41], [46] in PBF-LB/M components.

Modern high-fidelity multi-layer TMPS models follow a multiscale approach to analyse global residual stresses and distortions in AM parts [47-50]. Single-layer microscale models can be used to derive an equivalent heat source representing the melt pool. To account for scanning strategy effects, this is imposed to a hatch block in a mesoscale model [48], [49], [50]. The resulting temperature histories or inherent strains are further applied to a thermo-mechanical [49], [50] or a purely static mechanical [53], [54] macroscopic model, respectively. Element activation is either hatch block wise [48], or layer wise (superlayer approach) [53], [54] with the former approach being the best compromise between accuracy and numerical efficiency [55]. A coupled activation and heat input approach using event series as recently introduced in the commercial FE software Abaqus [49], [50] demonstrated excellent agreement between measured and predicted residual strains in the NIST AM Simulation Benchmark [56].

A simplified weakly-coupled TMPS model implemented in the commercial FE Software Ansys, uses a superlayer approach [57]. Thereby, superlayers, i.e. aggregates of actual powder layers represented by a finite element layer, are instantaneously activated layer-by-layer at close to melting temperature. The resulting temperature field following cooldown is applied in a subsequent mechanical simulation to predict the residual stresses that arise from the constrained thermal contraction. Despite significant simplifications of the complex physical phenomena on a local level, this industrially relevant approach allows to estimate residual stresses and distortions on a part-level at low numerical cost [58]. The accuracy of all outlined simulation approaches is strongly influenced by the underlying constitutive models describing the thermo-physical and thermo-mechanical behaviour of materials. Specifically, the thermal expansion has a significant impact on predicted residual stresses and distortions.

In the present study, a comprehensive model is introduced to describe the apparent build-direction dependent expansion strain in PBF-LB/M manufactured Ti-6Al-4V (Grade 23) in the as-build condition for Finite Element Analyses (FEA). Thereby, the isotropic thermal expansion strain ε_{th} is modelled independently from the transversally isotropic transformation strain ε_{tr}^{h} that arises from the $\alpha' \rightarrow \beta$ transformation during heating at > 850 °C. During cooldown, the transformation strain ε_{tr}^{c} resulting from the $\beta \rightarrow \alpha + \beta$ transformation is modelled as isotropic. In a first step, the model and its implementation as an UEXPAN subroutine for the FE software Abaqus are introduced. To demonstrate the effectiveness and relevance of the apparent expansion model and its implementation, it is applied 1) to predict the expansion in a 45° tilted cylinder, 2) to investigate the residual stresses in a single PBF-LB/M laser weld-track (single-layer TMPS model), and 3) to predict the distortion of a cantilever following stress relief after support structure removal (multi-layer TMPS model).

The availability of a FE simulation model able to account for the anisotropy of the apparent expansion is a prerequisite to investigate the impact of the experimental findings in [29], and to gain more detailed understanding of the underlying mechanisms generating residual stresses and distortion in PBF-LB/M-fabricated Ti-6Al-4V components. This is crucial for optimizing the mechanical integrity and dimensional stability of PBF-LB/M-fabricated Ti-6Al-4V components in engineering applications subjected to post processing heat treatments or high-temperature applications.

METHODS

MATERIAL & EXPERIMENTS

The apparent expansion model established in this study is based on findings presented in [29] on the build-orientation dependent apparent thermal expansion behaviour of Ti-6Al-4V as manufactured by PBF-LB/M.

Vertically and horizontally oriented cylindrical samples were printed on an Additive Industries Metal*FAB1* PBF-LB/M system in single laser mode applying the process parameters summarized in Table 1. The process was conducted under Ar atmosphere using build plate heating at 150 °C. Plasma atomized Ti-6Al-4V (Grade 23) powder was supplied with a chemical composition according to Table 2, an aspect ratio of D_{min}/D_{max} = 0.97, and a characteristic particle size distribution of D_{10} = 21 µm, D_{50} = 35 µm, and D_{90} = 49 µm.

Table 1 PBF-LB/M process parameters: Ti-6Al-4V (Grade 23).

Laser Power P [W]	**Scan Velocity v [mm/s]**	**Laser Spot Diameter d [mm]**	**Layer Thickness t [mm]**	**Hatch Spacing h [mm]**	**Hatch Angle α [°]**
365	1025	0.10	0.06	0.05	67° (rotating)

Dilatometry was further conducted on cylindrical (D8 mm × L120 mm) samples with vertical and horizontal build-orientation in the as-built condition. A NETZSCH DIL402 Expedis® Supreme dilatometer was used to measure the total thermally induced elongation under quasi-static conditions with a heating-rate of 5 K/min in an Ar atmosphere up to 1100 °C. Slow cooling to 450 °C was subsequently applied at a cooling-rate of 5 K/min. During the experiments a controlled measuring force of 0.2 N was maintained and a W standard material was used to correct for the thermal expansion of the measuring system.

Table 2 Chemical composition [%w]: Ti-6Al-4V (Grade 23, ASTM F3001) powder by AP&C.

Ti	**Al**	**V**	**Fe**	**O**	**C**	**N**	**H**	**Y**	**Others (each)**	**Others (total)**
bal.	6.32	4.03	0.21	0.10	0.01	0.01	0.002	<0.001	<0.1	<0.4

To verify the effectiveness of the thermal expansion model in the multi-layer thermo-mechanical process simulation, six cantilevers – i.e. three oriented along and three transverse to the Ar gas flow – were manufactured under the same conditions as the dilatometry samples. Subsequently, the support structure of the cantilevers was EDM wire-cut 1 mm above the substrate to release residual stresses according to the cut compliance method (CCM), see Fig. 1. The resulting distortion was measured along three lines (middle, left, right) at the top of the cantilever using a tactile coordinate measurement machine. Finally, an overall average was calculated for all measurements of the two respective cantilever orientations, i.e. along and transverse to the gas flow.

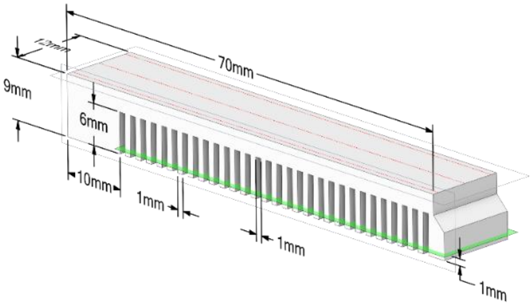

Fig. 1 Cantilever for validation of multi-layer TMPS according to the cut compliance method. Green: cutting plane. Red: measurement paths for distortions

MODELLING OF APPARENT EXPANSION

As outlined in [29], the apparent expansion ε_{exp} observed in the dilatometer experiments of as-printed Ti-6Al-4V varies significantly with the underlying build-orientation, Fig. 2. While the actual thermal expansion strain ε_{th} is independent of the build-orientation, the transformation strain ε_{tr}^{h} arising from the $\alpha' \rightarrow \beta$ transformation during heating at approximately 850 °C to 1000 °C varies strongly with the build-orientation, i.e. it is positive for vertically and negative for horizontally built samples. During cooldown from the fully transformed β phase to $\alpha + \beta$, the resulting transformation strain ε_{tr}^{c} can be considered as isotropic.

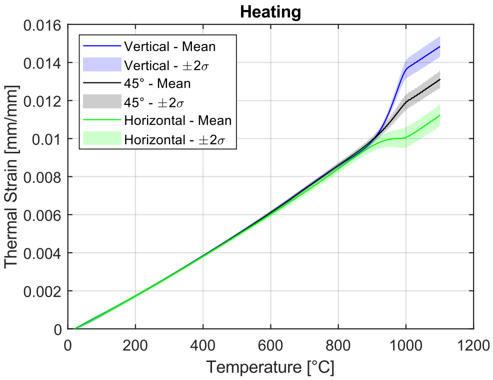

Fig. 2 Apparent expansion for three build-orientations as determined from dilatometry [29]

Following these experimental observations, a model to describe the total apparent expansion needs to account for

1) path-dependency, i.e. differing behaviour during heating and cooling
2) isotropic thermal expansion
3) transversally isotropic transformation strain during heating, and
4) isotropic transformation strain during cooling.

Consequently, the total apparent expansion strain ε_{exp} in longitudinal (L) and transverse (T) direction is additively decomposed into an isotropic thermal expansion strain ε_{th} and a transversally isotropic transformation strain during heating (h) – i.e. $\varepsilon_{tr,L}^{h}$ and $\varepsilon_{tr,T}^{h}$, respectively – and an isotropic transformation strain during cooling (c) – i.e. ε_{tr}^{c} according to Eq. (1).

Heating (dT > 0)

$$\varepsilon_{exp,L}^{h}(T) = \varepsilon_{th}(T) + \varepsilon_{tr,L}^{h}(T) \tag{1a}$$

$$\varepsilon_{exp,T}^{h}(T) = \varepsilon_{th}(T) + \varepsilon_{tr,T}^{h}(T) \tag{1b}$$

Cooling (dT < 0)

$$\varepsilon_{exp,L}^{c}(T) = \varepsilon_{th}(T) + \varepsilon_{tr}^{c}(T) \tag{1c}$$

$$\varepsilon_{exp,T}^{c}(T) = \varepsilon_{th}(T) + \varepsilon_{tr}^{c}(T) \tag{1b}$$

Longitudinal $\varepsilon_{tr,L}^{h}$ and transverse $\varepsilon_{exp,T}^{h}$ transformation strains are determined from dilatometry on vertically and horizontally oriented PBF-LB/M samples, respectively. To discriminate between heating and cooling paths, the temperature increment dT is evaluated, indicating heating if positive and cooling if negative. For constant temperatures, i.e. dT = 0, the increment of the apparent expansion strain is neutral dε_{exp} = 0.

The isotropic thermal expansion strain ε_{th} is modelled using a third-order polynomial

$$\varepsilon_{th}(T) = p_3(T - T_0)^3 + p_2(T - T_0)^2 + p_1(T - T_0) \tag{2}$$

Therein, T_0 denotes the reference temperature which is defined as 20 °C throughout this study. p_1 to p_3 describes the polynomial coefficients.

The transversally isotropic transformation strain ε_{tr} is modelled using two state functions, i.e. $\phi^{h}(T)$ and $\phi^{c}(T) \in [0, 1]$, which reflect the progress of the $\alpha' \rightarrow \beta$ transformation during heating and the $\beta \rightarrow \alpha + \beta$ transformation during cooling, respectively. Inspired by the experimental characteristic of the apparent expansion ε_{exp}, the temperature dependent transformation strain is modelled as the product of a constant transformation strain ε_0 and the respective temperature dependent state function acting as a weighting function.

$$\varepsilon_{tr}^{h}(T) = \varepsilon_0^{h}\phi^{h}(T) \tag{3a}$$

$$\varepsilon_{tr}^{c}(T) = \varepsilon_0^{c}(\phi^{c}(T) - 1) \tag{3b}$$

Eq. (3) is valid both for L and T components, whereas ε_0 differs for the L and T components during heating assuming transversal isotropy – i.e. $\varepsilon_{0,L}^{h} \neq \varepsilon_{0,T}^{h}$ – while it is assumed isotropic during cooling – i.e. $\varepsilon_{0,L}^{c} = \varepsilon_{0,T}^{c}$. The different transformation characteristics during heating and cooling are thereby accounted for by separate state functions – i.e. $\phi^{h}(T) \neq \phi^{c}(T)$.

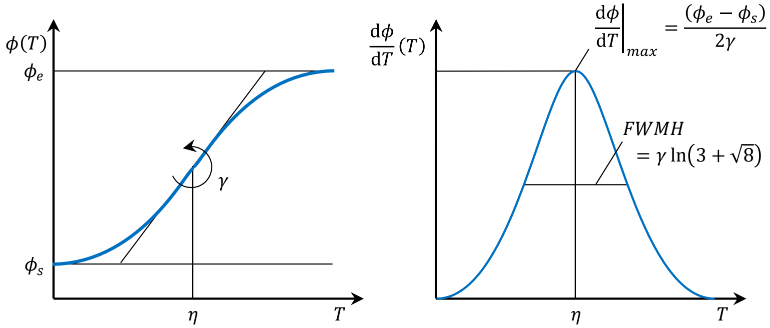

Fig. 3 Schematic illustrating the state functions ϕ(T) and their temperature derivative

In agreement with the experimental dilatometry [29], a sigmoid function, specifically a generalized $tanh$-function, is adopted for the state functions $\phi(T)$ showing the best agreement between model and experimental data.

$$\phi(T) = \phi_s + \frac{1}{2}(\phi_e - \phi_s)\left(\tanh\left(\frac{T-\eta}{\gamma}\right) + \tanh\left(\frac{\eta}{\gamma}\right)\right) \qquad (4)$$

Considering, that the $tanh$-function can be interpreted as a cumulative density function (CDF), i.e. the integral, of a $sech$ probability density function (PDF), the model parameters can be readily interpreted, see Fig. 3:

- η corresponds to the temperature at the peak of the PDF or the turning point of the CDF [°C]
- γ is associated with the width of the peak of the PDF (FWMH – Full Width at Mean Height) or the maximum slope of the transition from 0 to 1 in the CDF [°C]
- ϕ_s corresponds to the value of the state variable at $T \ll \eta$, i.e. the lower asymptote of the CDF [-]
- ϕ_e corresponds to the value of the state variable at $T \gg \eta$, i.e. the upper asymptote of the CDF [-]

The temperature characteristic of the transformation strain is fully described by $\phi(T)$ in Eq. (4). Both for heating and cooling, the lower and upper asymptotes of the state functions were defined as $\phi_s = 0$ and $\phi_e = 1$, respectively. Due to the different characteristics of the transformation during heating and cooling, the model parameters η and γ differ - i.e. η^{h}, γ^{h}, for ϕ^{h} and η^{c}, γ^{c} for ϕ^{c}. For simplicity, the directional dependence of the transformation strain is fully described by different ε_0 values for L and T.

To make this model available for FE simulations, an user-subroutine UEXPAN has been developed for the commercial FE software Abaqus. The UEXPAN needs to provide the increment of the apparent expansion strain $\Delta\varepsilon_{exp}$ (i.e. EXPAN) over a time increment and for all relevant directional components. Thereby, it can be accounted for dependencies of the expansion strain both on temperature and internal state functions. In addition, UEXPAN allows to model orthotropic thermal expansion, when increments of the expansion strain are provided in three orthogonal directions of a material coordinate system, i.e. $\Delta\varepsilon_{exp,11}$, $\Delta\varepsilon_{exp,22}$, and $\Delta\varepsilon_{exp,33}$. By defining two components as equivalent, e.g. $\Delta\varepsilon_{exp,11} = \Delta\varepsilon_{exp,22} = \Delta\varepsilon_{exp,T}$ and different to a third component $\Delta\varepsilon_{exp,33} = \Delta\varepsilon_{exp,L}$, a transversally isotropic expansion can be realized.

In addition to the incremental form of the expansion model defining EXPAN, the user subroutine also allows to define differential strains as temperature derivatives (DEXPANDT).

$$\frac{\mathrm{d}\varepsilon_{exp}}{\mathrm{d}T}(T) = \frac{\mathrm{d}\varepsilon_{th}}{\mathrm{d}T}(T) + \frac{\mathrm{d}\varepsilon_{tr}}{\mathrm{d}T}(T) \tag{5a}$$

$$\frac{\mathrm{d}\varepsilon_{th}}{\mathrm{d}T}(T) = 3p_3(T - T_0)^2 + 2p_2(T - T_0) + p_1 \tag{5b}$$

$$\frac{\mathrm{d}\varepsilon_{tr}}{\mathrm{d}T}(T) = \varepsilon_0 \, \frac{\mathrm{d}\phi}{\mathrm{d}T}(T) = \frac{\varepsilon_0}{2\gamma}\left(\phi_e - \phi_s\right)\mathrm{sech}^2\left(\frac{T-\eta}{\gamma}\right) \tag{5c}$$

Model Parameter Identification

Due to the readily interpretable form of the expansion model, the model parameters can be directly determined from an analysis of dilatometer data. Thereby, dilatometer measurements on vertically built samples are used to determine the parameters for the L-components, while data from horizontally built samples yield the parameters for the T-components of the expansion model. The following data analysis routine was implemented in MATLAB to determine the nine remaining model parameters.

- **Data Preparation**
  All apparent expansion strain measurements were resampled every 1 °C at equal temperatures. First and second temperature derivatives were calculated and smoothed using local quadratic regression (*loess*) and a 10% span of the data vector.
- **Background Subtraction**
  Based on the first derivative of the apparent expansion strain, $\mathrm{d}\varepsilon_{exp}/\mathrm{d}T$, the peak was identified and removed between 780 °C and 1050 °C (heating) and between 805 °C and 940 °C (cooling), respectively. The remaining data was then fitted with a second order polynomial and shifted to form an overall mean curve, i.e. the background ($\mathrm{d}\varepsilon_{\mathrm{th}}/\mathrm{d}T$). The background is subtracted from the $\mathrm{d}\varepsilon_{exp}/\mathrm{d}T$ curve leaving the first derivative of the transformation strain $\mathrm{d}\varepsilon_{tr}/\mathrm{d}T$.
- **Peak Analysis**
  The peaks of the $\mathrm{d}\varepsilon_{tr}/\mathrm{d}T$ curve ($sech$-PDF) are identified, characterising the turning points in the state functions $\phi(T)$ ($tanh$-CDF). The temperature at the peak defines the model parameter η, while γ is determined from its $FWMH = \gamma \ln\left(3 + \sqrt{8}\right)$, and the transformation strain $\varepsilon_0 = 2H\gamma$ from the peak height H.

- **Parameter Optimisation**
  Following a first analytical identification of the model parameters an overall model fit using the MATLAB optimizer *fmincon* was applied to improve overall accuracy.

Fig. 4 shows a comparison of the respective model predictions using analytically determined model parameters (green line) with measured apparent expansion data (black circles) and the optimized model (red line). In addition, the first derivatives of the thermal and the transformation strains are shown, underpinning the already good agreement of the analytical approach. The optimized model parameters are listed in Table 3 and Table 4.

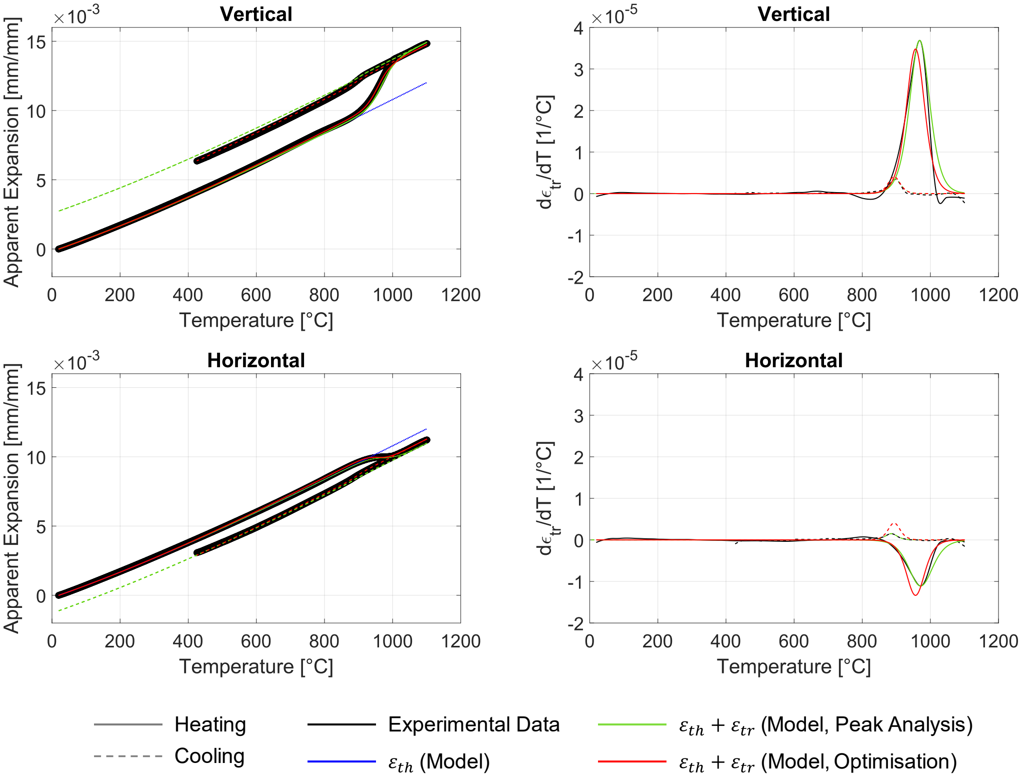

Fig. 4 Comparison of measured apparent expansion strain (black circles) with model predictions using parameters 1) as analytically determined (green) and 2) as optimised (red). The right column shows the first derivative of the transformation strains $d\varepsilon_{tr}/dT$ after background subtraction.

Table 3 Optimised model parameters for thermal strain model $\varepsilon_{th}(T)$, cf. Eq. (2).

p_3	p_2	p_1
-1.3170e-12	3.9358e-09	8.6217e-06

Table 4 Optimised model parameters for transformation strain model $\varepsilon_{tr}(T)$, cf. Eq. (3) and (4).

	ε_0^h	η_h	γ_h	ε_0^c	η_c	γ_c
L	2.5141e-03	956.39	36.12	3.8683e-04	893.50	23.7937
T	-9.6401e-04	956.39	36.12	3.8683e-04	893.50	23.7937

SIMULATION MODELS

To demonstrate the effectiveness and relevance of the presented expansion model, three simulations have been implemented, Fig. 5. All simulations were conducted using Abaqus/CAE 2024. The Fortran based UEXPAN user-subroutine was implemented in Microsoft Visual Studio 2022 and compiled using the Intel Fortran Compiler 2019 following the guidelines in [59], [60].

First, the correct implementation of the UEXPAN has been verified by simulating the dilatometer experiment for vertically and horizontally oriented cylinders as used for the model parameter identification. Additionally, the predictive performance of the model is shown for a specimen tilted at 45° with respect to the vertical and horizontal directions used for model calibration.

To further demonstrate the relevance of an anisotropic expansion model accounting for thermal and transformation strains, a weakly-coupled single-layer thermo-mechanical process simulation (TMPS) model of a single PBF-LB/M laser weld track was implemented. Simulated stresses from a model assuming isotropic thermal expansion only are compared to a model assuming the presented expansion model which accounts for transversally isotropic transformation strains.

Finally, a weakly-coupled multi-layer TMPS model was implemented to compare simulated and experimentally determined distortions in a PBF-LB/M printed cantilever after stress relief following support structure removal. It is investigated if the presented expansion model reasonably predicts the residual stresses introduced during the PBF-LB/M process.

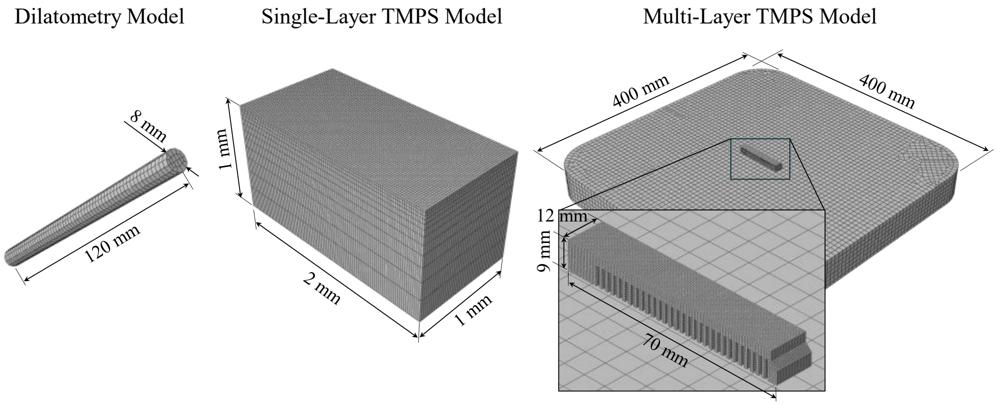
Dilatometry Model Single-Layer TMPS Model Multi-Layer TMPS Model

Fig. 5 Simulation models

Dilatometry Model

To simulate the apparent expansion as measured in the dilatometer experiment conducted in [29], a cylinder with 8 mm diameter and 120 mm length was subjected to a thermal heating and cooling cycle (20°C - 1100°C - 20°C) in an implicit static/general procedure.

The 3D cylinder was meshed using 1200 linear hexahedral elements with reduced integration (C3D8R), see Fig. 5 (left).

A local rectangular coordinate system was created to define the material orientation with the 3-direction corresponding to the L orientation and the 1- and 2- directions referring to the T orientation of the expansion model. By orientating the cylinder either along the 3-direction, the 1- or 2- direction, or along the space diagonal, vertical, horizontal, and 45° tilted build orientations were realized.

The mechanical boundary conditions were defined such that an unconstrained expansion was ensured both in longitudinal and transverse directions. Thereby, the build-up of stresses during the thermal cycle was prevented.

Time incrementation was chosen such that the maximum temperature increment was limited to 5 °C. Like this it was ensured that pronounced change of transformation strains during the $\alpha' \rightarrow \beta$ transformation was appropriately resolved.

Single-Layer TMPS Model (Weld Track)

To investigate the relevance of the presented expansion model, a weakly-coupled single-layer TMPS model of a single 1.2 mm PBF-LB/M weld track was set-up using a volumetric Gauss-Goldak heat input model [51] following the approach and using the model parameters outlined by [61], [62] with a trajectory-based event-series implementation provided by Abaqus [50].

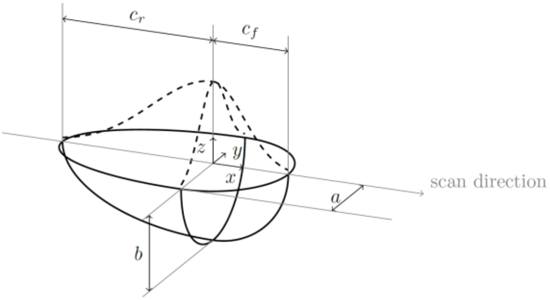

Fig. 6 Schematic illustrating geometric Gauss-Goldak parameters

For simplicity, only bulk material was considered, and material activation was neglected. This reflects a situation in which an already solidified AM part is exposed to laser irradiation, assuming powder layer properties to be equivalent to bulk properties. The substrate was meshed using 60000 linear (D)C3D8R elements with lateral dimensions of 20 µm × 20 µm and a vertical bias ranging from 20 µm to 200 µm over a depth of 1 mm, see Fig. 5 (middle).

In a first transient heat transfer simulation, the heat input introduced by a scanning laser source (laser power 250 W, laser spot diameter 100 µm) was modelled using a volumetric Gauss-Goldak heat flux which is scanned with a speed of 600 mm/s in 1-direction (T). The geometric Gauss-Goldak parameters, see Fig. 6, were defined as a = 50 µm (half width), b = 30 µm (depth), c_f = 50 µm (frontal half axis along laser path), and c_r = 117 µm (rear half axis along laser path) with energy fractions of f_f = 0.6 and f_r = 1.4 [61], [62]. The laser absorptivity was defined as $\eta = 0.55$ and the HTC on top of the plate as 0.02 W/m^{2}K. The resulting instantaneous temperature distribution at the end of the 1.2 mm single PBF-LB/M weld track is illustrated in Fig. 7. As the process parameters and heat-source was adopted from literature and thus not directly calibrated to experimental data, the resulting maximum temperature of > 7300 °C is significantly above melting temperature and thus not considered as realistic. The goal of the present simulation is, however, to provide a relative comparison of residual stresses in the near-field beyond the melt pool as predicted by a model using a simple isotropic thermal expansion coefficient and one that uses the expansion model presented in this study. Thus, the adopted model is judged as sufficient for this purpose.

Following the thermal simulation, the temperature field is imposed to two different mechanical models, i.e. one using a simple thermal expansion coefficient CTE (Fig. 10, right) representing isotropic thermal strain only, and another using the UEXPAN expansion model presented here that accounts for the transversely isotropic transformation strains.

Both, the thermal and the mechanical simulation models used a minimum time increment Δt_{min} of $5 \cdot 10^{-7}$ s and a maximum time increment of Δt_{max} of 10^{-5} s for the simulated time period of $2 \cdot 10^{-3}$ s.

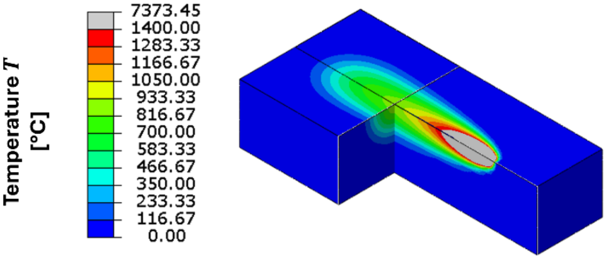

Fig. 7 Instantaneous temperature distribution in single-track PBF-LB/M weld after 1.2 mm

Multi-Layer TMPS Model (Cantilever)

To model the build-up of residual stresses in a cantilever manufactured by PBF-LB/M, a multi-layer TMPS model was implemented in Abaqus using event-series for the layer-wise element activation [50] following the industrially well-established superlayer approach by Ansys [57]. Thereby, a finite element layer, i.e. superlayer (500 µm), represents multiple powder layers (60 µm). Conventionally, these are activated successively at a temperature close to the melting temperature, e.g. 1100 °C, followed by a cooldown phase. Further assuming a reference temperature for the thermal expansion/contraction at the same activation temperature, residual stresses are introduced by constrained shrinkage only. As the build orientation dependent transformation strains occur during heating, a modified approach was additionally adopted within this study:

- Activation of superlayer at room temperature within $4.9\cdot10^{-5}$ s (quasi-instantaneous)
- Heating of superlayer to 1100 °C within $4.9\cdot10^{-4}$ s (i.e. time to scan superlayer)
- Cooling of superlayer within 91.7 s (i.e. dwell and recoating time for superlayer)

This allows to account for additional residual stresses that arise from the transversally isotropic transformation strains as well as from constrained heating. Following the cooldown of the last layer, the support structure of the cantilever is cut at a height of 1 mm using a model change that deactivates a pre-defined element set. The resulting deflection of the cantilever after stress relief following support removal reflects the extent of the residual stresses introduced in the PBF-LB/M process.

Four model variants are compared within this study: 1) conventional approach + thermal strains, 2) conventional approach + thermal and transformation strains, 3) modified approach + thermal strains, and 4) modified approach + thermal and transformation strains. Thereby, the process parameters defined in Table 1 are assumed for the calculation of superlayer heating- and cooling-times.

The cantilever was meshed using 44255 linear (D)C3D8 elements with dimensions 500 µm × 500 µm × 500 µm, see Fig. 5 (right). It was tied to a 400 mm × 400 mm × 45 mm substrate plate which was discretized using 25745 (D)C3D8 elements with an approximate size of 7 mm × 7 mm × 7 mm.

Following the thermal simulation, the temperature field is imposed to the mechanical model following a weak-coupling approach. Both, the thermal and the mechanical simulation models used a fixed time increment Δt of $4.9 \cdot 10^{-6}$ s in the heating phase allowing to resolve temperature changes in the order of 10 °C per increment, i.e. 1% of the maximum temperature.

Material Properties

Following [62], [63], all simulation models used thermo-physical data by [64] and thermo-mechanical data by [65]. Thermal expansion coefficients (CTE) considering thermal strains only were derived from the dilatometry data in [29] using the model given by Eq. (2) with the optimised parameters listed in Table 3. The simulation models considering the combined thermal and transformation strains used the UEXPAN subroutine with the optimised model parameters listed in Table 4 instead.

Fig. 8 shows the heat capacity, thermal conductivity, and density for bulk Ti-6Al-4V. To model the effect of the phase transformations on the temperature evolution, latent heats were defined as follows [62], [63], [64]:

- solid-solid ($\alpha' \rightarrow \beta$) phase transformation ($T_s$ = 980 °C, T_e = 1010 °C) 4.8·J/g
- solid-liquid phase transformation (T_s = 1604 °C, T_e = 1660 °C) 268·J/g
- liquid-vapor phase transformation (T_s = 3290 °C, T_e = 3390 °C) 983·J/g

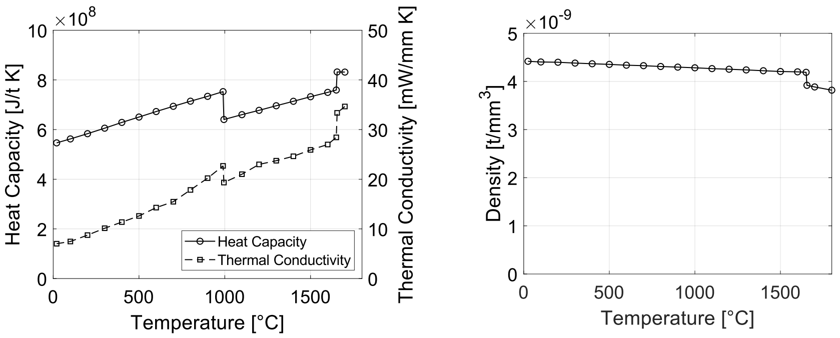

Fig. 8 Thermo-physical properties used for simulation model as adopted from [64]

Fig. 9 shows the temperature dependent elastic modulus and Poisson ratio as well as the yield stress for bulk Ti-6Al-4V according to [65]. Plasticity was implemented using a multilinear kinematic hardening model to appropriately account for the Bauschinger affect. To ensure numerical stability, low non-zero mechanical properties were defined beyond the melting temperature at 1600 °C.

As required by Abaqus, the UEXPAN subroutine presented in this study provides expansion strain increments which consist of thermal and transformation strain increments.

To demonstrate the impact of the expansion model, the respective simulation results were compared to simulations using isotropic thermal expansion according to Eq. (2) only. As Abaqus requires the definition of temperature dependent mean CTEs in this case, these were derived from the measured thermal strains, see Fig. 10 (left), using the difference quotient according to [66]. Fig. 10 (right) compares the mean CTE of this study with data used by [63].

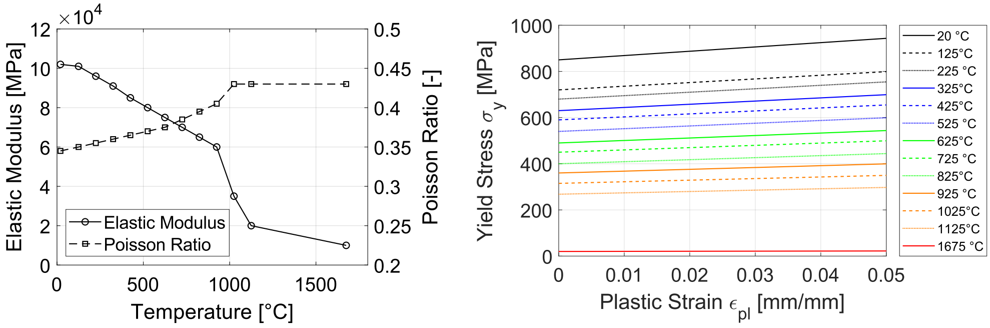

Fig. 9 Thermo-mechanical properties used for simulation model as adopted from [65]

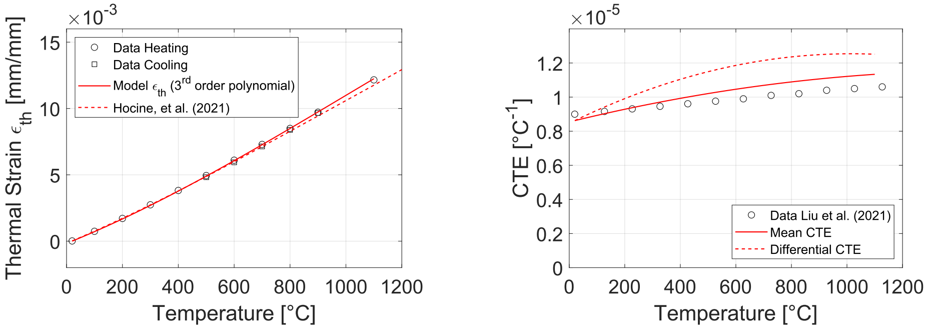

Fig. 10 Measured and modelled thermal strain (left) and mean CTE (right) used for the simulation models accounting for thermal strain only in this study. Comparison to literature data [62], [63]

RESULTS AND DISCUSSION

Anisotropic Apparent Expansion

The expansion model described by Eq. (1) to (4) was fitted to experimental apparent expansion data of vertically and horizontally built PBF-LB/M samples [29], yielding the optimised model parameters for the longitudinal (L) and transverse (T) directions in Table 3 and Table 4. Recalculation of the dilatometry experiments using the expansion model implemented as UEXPAN demonstrates excellent agreement between simulation and experimental data verifying the correct implementation of the model, see Fig. 11 (left, middle). The expansion model was further applied to predict the apparent expansion in a PBF-LB/M sample printed under a 45° tilt angle which was not used for model calibration. Fig. 11 (right), shows again excellent agreement between the (unseen) experimental data and the model prediction, underpinning the solid predictive performance of the presented expansion model.

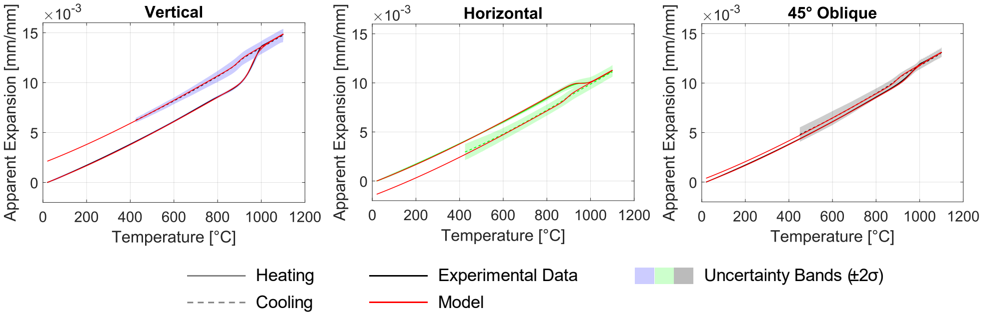

Fig. 11 Comparison of measured apparent expansion strain with UEXPAN model predictions for vertically, horizontally, and 45° oriented cylindrical dilatometer samples

The findings in [29] show that the apparent difference in the expansion behaviour of vertically and horizontally built samples originates from the morphological and crystallographic texture of Ti-6Al-4V manufactured by PBF-LB/M. Prior β grains grow epitaxially with their $\langle 001\rangle_\beta$ direction along the thermal gradient, i.e. effectively along the build-direction. During cooldown, α' laths precipitate on the prior β grain boundaries obeying the Burgers orientation relationship and growing along the invariant directions $\langle 335\rangle_\beta$ to minimise internal energy. This results in a particular acicular martensitic morphology with α' laths being oriented at a 35 to 55° angle to the prior β grain boundaries. During the $\alpha' \rightarrow \beta$ transformation, crystallographic transformation strains occur that macroscopically manifest themselves in positive transformation strains along the major axis of the prior β grains, and negative transformation strains along the minor axis.

The investigation by [29] has shown that the transformation strain for the $\alpha' \rightarrow \beta$ transformation (heating) is 0.271% in L (vertical) direction and -0.084% in T (horizontal) direction, while it is -0.037% in L (vertical) direction and -0.013% in T (horizontal) direction for the $\beta \rightarrow \alpha + \beta$ transformation (cooling). This is in excellent agreement with the optimized model parameters $\varepsilon^h_{0,L}$ = 0.251% and $\varepsilon^h_{0,T}$ = -0.096% for heating, and $\varepsilon^c_{0,L} = \varepsilon^c_{0,T}$ = -0.039% for the cooling phase, see Table 4. The minor differences arise from the simplified $tanh$-approach adopted for the state functions ϕ^h and ϕ^c .

Furthermore, the model parameters for the polynomial model to describe the thermal strain appear to differ significantly from the results presented in [29]. Both parameter sets represent the experimental data very well, however, and the differences are merely a consequence of the overall model fit in this study vs. the simple data analysis conducted in [29].

In conclusion, the UEXPAN implementation of the presented expansion model is verified, and its robust predictive performance is shown. Furthermore, the optimized model parameters are in excellent agreement with the experimental observations in [29].

Comparison of Residual Stresses in a Single PBF-LB/M Weld Track

While the expansion model presented in this study well represents the apparent expansion observed in dilatometry experiments, the question arises as to its relevance for practical applications relative to the adoption of a simpler approach accounting for thermal strains only. To study the development of residual stresses during the PBF-LB/M process, both expansion models are compared using a single-layer TMPS simulation of a single PBF-LB/M weld track. Such a simulation model can for instance be used to analyse stresses in the near-field of the melt pool and optimise scan strategies that minimize residual stresses and distortions.

Fig. 12 shows a comparison of the normal stress components and the accumulated plastic strain of a single-layer TMPS model accounting for isotropic thermal strains ε_{th} only (left column), and one that accounts for both isotropic thermal ε_{th} and transversally isotropic transformation strains ε_{tr} (right column). The model considering thermal strains only can be interpreted to reflect the situation in a conventionally manufactured Ti-6Al-4V material volume, while the model accounting for the anisotropic transformation strains represents the situation in a solidified material volume after PBF-LB/M processing. While the stress distributions are qualitatively comparable with relative differences in the in-plane longitudinal and transverse stresses < 4 %, the maximum and minimum vertical stresses are predicted to be approximately 9 % smaller and 9% larger, respectively, by the isotropic ε_{th} model than by the transversally isotropic $\varepsilon_{th} + \varepsilon_{tr}$ model, see Table 5. The maximum compressive vertical stresses are very localised to the starting point of the weld track and may arise from the enhanced expansion in build-direction and reduced in-plane expansion during the $\alpha' \rightarrow \beta$ transformation given the severe initial temperature gradients. Despite these localized differences, the accumulated plastic strain is approximately 90% larger in the ε_{th} model than in the $\varepsilon_{th} + \varepsilon_{tr}$ model along the whole weld track.

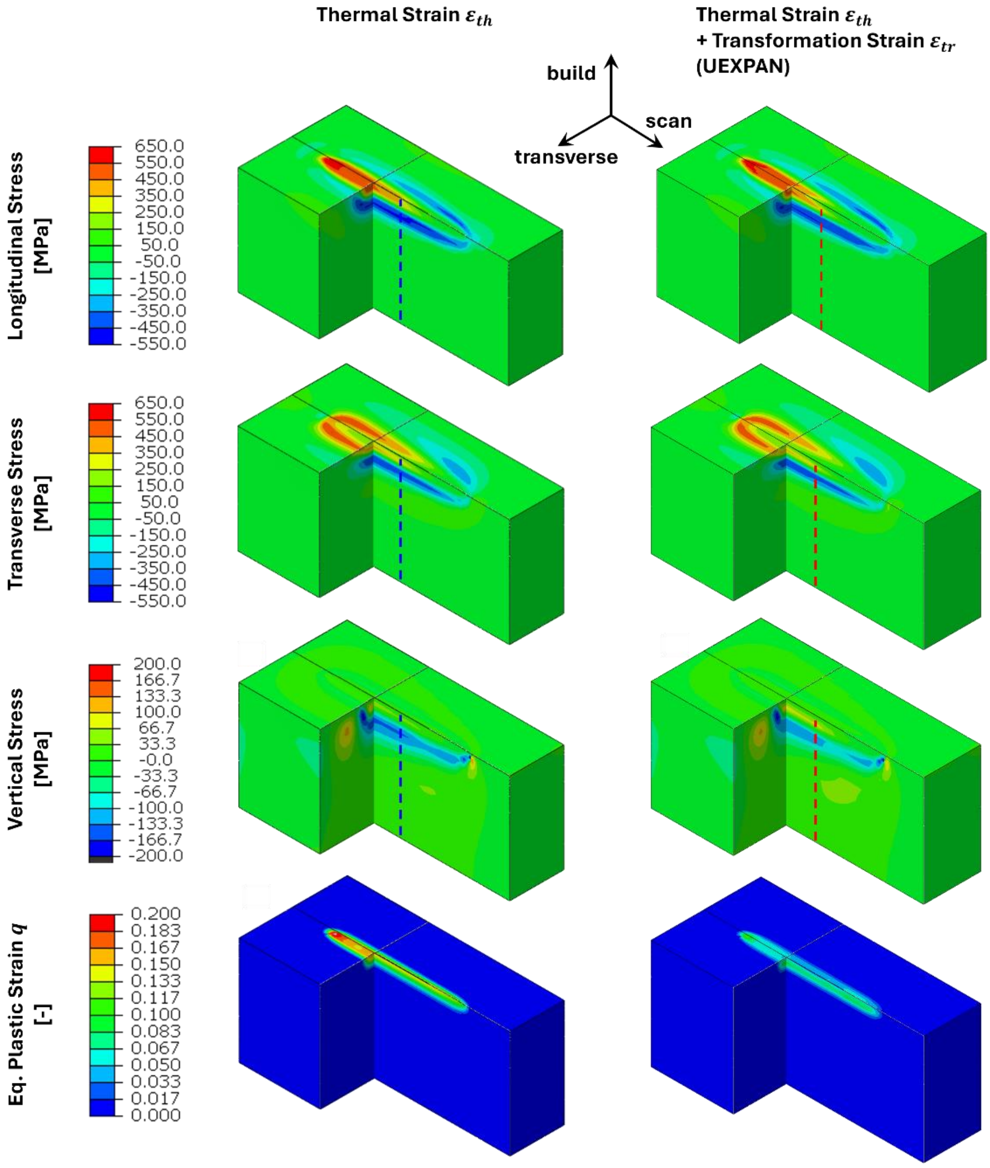

Fig. 12 Comparison of stress components and accumulated equivalent plastic strain in a single-track PBF-LB/M weld in longitudinal, transverse, and vertical (i.e. build-direction) directions with respect to the scanning direction as predicted by models accounting for thermal strain only (left column) and considering thermal and transformation strains using an UEXPAN subroutine (right column). Paths (blue, red) indicate evaluation region for stresses shown in Fig. 13

Table 5 Comparison of simulated max/min normal stress components as predicted by models accounting for ε_{th} and $\varepsilon_{th} + \varepsilon_{tr}$, respectively.

Stress	**ε_{th} model**	**$\varepsilon_{th} + \varepsilon_{tr}$ model (UEXPAN)**	**Relative Difference**
Longitudinal	665 MPa	663 MPa	-0.3 %
	-524 MPa	-526 MPa	0.3 %
Transverse	549 MPa	543 MPa	1.1 %
	-435 MPa	-417 MPa	-4.3 %
Vertical	185 MPa	170 MPa	-8.8 %
(Build-Direction)	-266 MPa	-292 MPa	8.6 %

To better understand these findings, the stress-temperature characteristics have been investigated at three depths - i.e. 75 µm, 115 µm, and 160 µm - along a vertical path in the centre of the weld track, see Fig. 12, that can be considered to be in steady-state. Considering a melting temperature of approximately 1650 °C, these points are located just below the anticipated melt pool. Fig. 13 shows that in-plane (longitudinal, transverse) and vertical normal stress components appear to be well comparable for the locations closest to the melt pool at a depth of 75 µm reaching temperatures > 1500 °C, and furthest away at 160 µm reaching < 500 °C. At the intermediate depth of 115 µm, however, the in-plane stresses predicted by the ε_{th} model are transitioning from compression to tension during a complete heat-up and cooldown cycle, while the stresses predicted by the $\varepsilon_{th} + \varepsilon_{tr}$ model remain in compression. In contrast, the vertical stresses predicted by the ε_{th} model first peak in compression before becoming tensile after reaching the peak temperature, while the peak compressive stress predicted by the $\varepsilon_{th} + \varepsilon_{tr}$ model is significantly smaller and the stress at the final temperature becomes neutral.

Initial compressive stresses during heat-up arise from the thermal expansion which is locally constrained by the surrounding material volume at lower temperatures, i.e. further away from the melt pool. As the temperature equilibrates, the hotter surrounding material, i.e. closer to the melt pool, starts pulling on initially colder material up to a point where stresses become tensile. As the transient temperature history has been considered the same for both models, the difference must be due to the transversally isotropic transformation strain considered in the $\varepsilon_{th} + \varepsilon_{tr}$ model. Apparent in-plane expansion strains are reduced with respect to the mere isotropic thermal expansion strains. Thus, the pull exerted by the surrounding material during temperature equilibration in the longitudinal and transverse directions is reduced leading to a reduced tendency of the stresses at a depth of 115 µm to turn tensile. Due to the increased apparent expansion in vertical direction, on the other hand, warmer surrounding material tends to keep the material volumes below under compression as predicted by the $\varepsilon_{th} + \varepsilon_{tr}$ model.

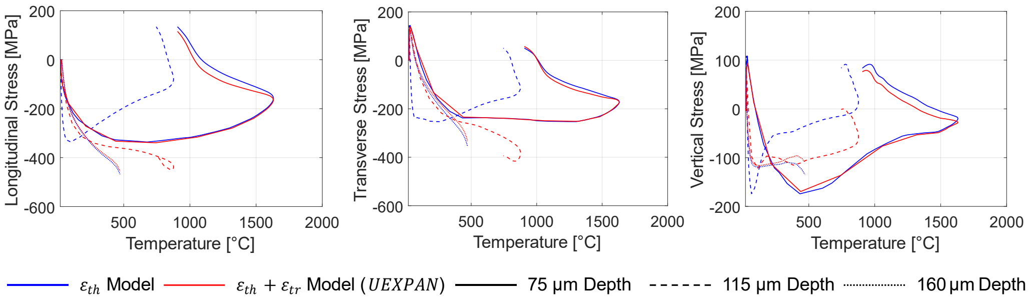

Fig. 13 Comparison of stress-temperature paths at three depths, i.e. 75 µm, 115 µm, and 160 µm along a vertical path (see Fig. 12) in the centre of a single-track PBF-LB/M weld

While not being experimentally validated, these results clearly show that accounting for the transversal isotropy induced by the transformation strains leads to relevant impacts on predicted stress distributions which need to be considered to better understand the residual stresses induced during the PBF-LB/M process.

Comparison of Distortions in Cantilever

In the following, distortions as measured in a cantilever after support removal (cutting) are compared to model predictions using a multi-layer TMPS approach. Besides comparing two expansion models, i.e. one accounting for thermal strains ε_{th} only, and a model accounting for both thermal and transformation strains $\varepsilon_{th} + \varepsilon_{tr}$ using the UEXPAN subroutine, two variants of the multi-layer TMPS approach are investigated, i.e. a conventional approach considering cooldown only, and a modified approach considering heat-up and cooldown.

The multi-layer TMPS approach has been widely adopted in industry for a first-level estimation of residual stresses and distortions of critical PBF-LB/M parts due to its numerical efficiency. Conventionally, finite element layers representing several powder layers are instantaneously activated directly at close to melting temperature. Residual stresses are thereby introduced during cooldown through constrained thermal shrinkage. The heating phase is neglected as justified by its much shorter duration and the exceeding of the melting temperature which would erase residual stresses that arise during heat-up. As the complex melt-pool physics and the respective transient thermal history are not accounted for, the activated layer can basically be regarded as a means of introducing thermal loading to the solidified layers below.

Fig. 14 shows that with the conventional approach (dashed lines) and for both expansion models, the predicted maximum vertical distortion is significantly larger with 5.7 mm than the measured values of 2.6 mm. The simpler isotropic ε_{th} model and the transversally isotropic $\varepsilon_{th} + \varepsilon_{tr}$ model deviate by only 0.01 mm. As the two models merely differ by the isotropic transformation strain of the $\beta \rightarrow \alpha + \beta$ transformation during cooldown, this can be concluded to be negligible.

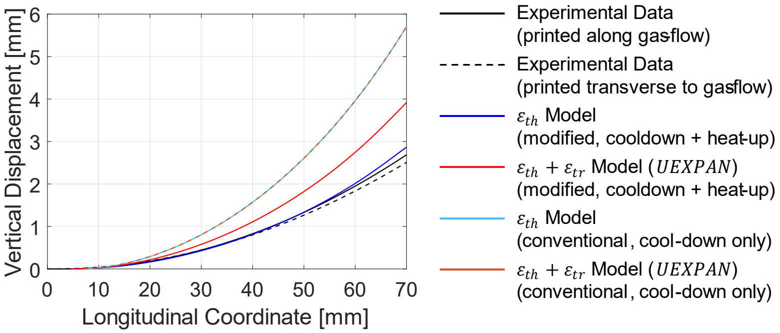

Fig. 14 Comparison of measured (black) and simulated distortions in a cantilever after support removal. Expansion models considered isotropic thermal strain only (blue, cyan) and thermal and transversally isotropic transformation strains by using the UEXPAN subroutine (red, orange)

To improve the model prediction, a modified multi-layer TMPS approach was implemented which considers activation at room temperature, followed by heating within ca. 0.5 ms, and cooling for ca. 90 s. Fig. 14 shows a significant improvement in both model predictions with the modified multi-layer TMPS approach. While the $\varepsilon_{th} + \varepsilon_{tr}$ model predicts a maximum vertical deflection of 3.9 mm, the ε_{th} model is unexpectedly more accurate with a deflection of 2.9 mm (+11 %). This result was verified using both finer spatial and temporal discretisations.

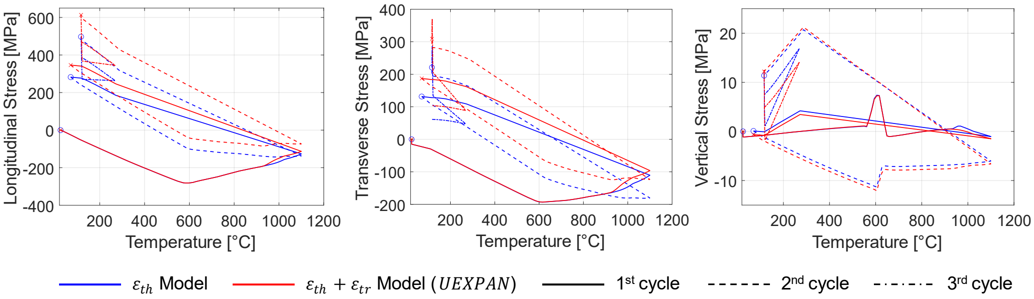

Fig. 15 Comparison of predicted stress-temperature characteristics at the centre of the cantilever, 2.5 mm below the top surface for initial heating (1st cycle) and two successive re-heating cycles (2nd and 3rd cycle)

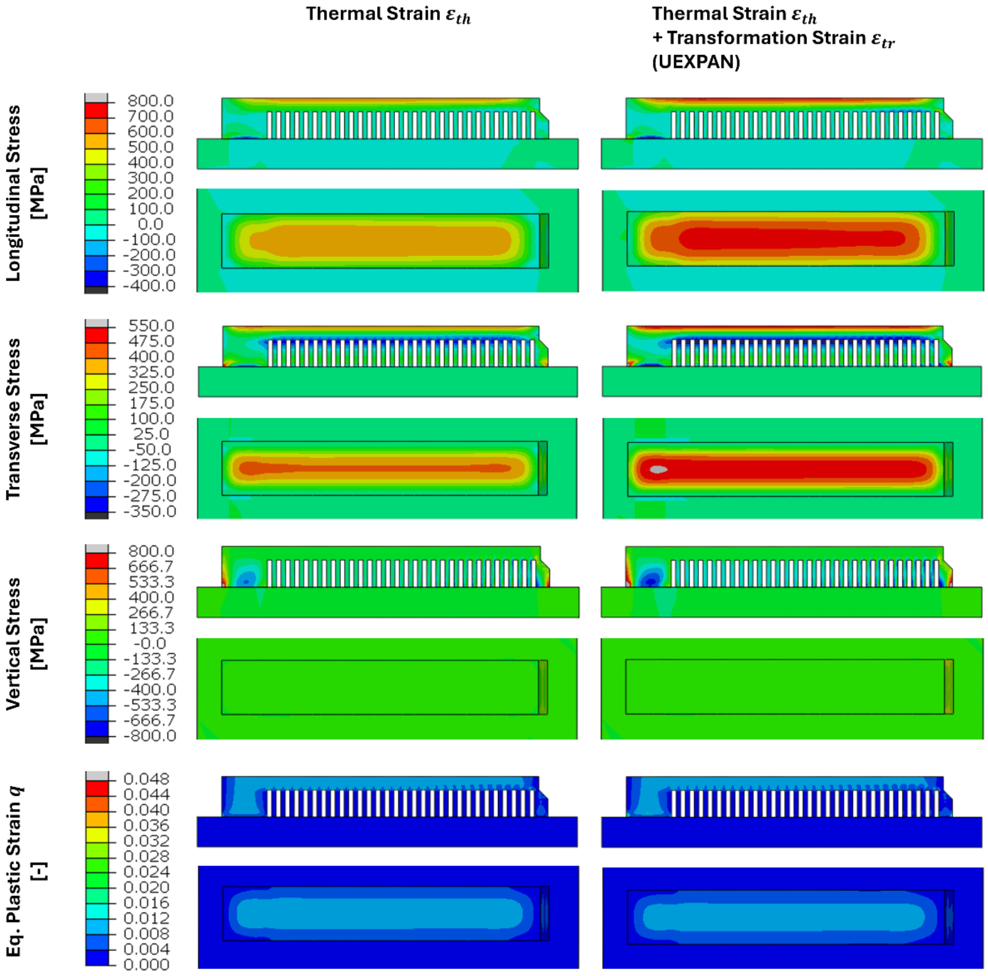

Fig. 16 Comparison of normal stress distributions in a cantilever prior to cutting for a model considering thermal strain only (left column) and a model considering thermal and transformation strains using a UEXPAN subroutine (right column). The top side-view image refers to a longitudinal cut through the cantilever centre, while the bottom image refers to the top view.

Fig. 15 shows the stress-temperature characteristics at the centre of the cantilever, 2.5 mm below the top surface. The impact of the transversally isotropic transformation is clearly visible in the first and second heating cycle at 900 °C to 1100 °C. In this temperature regime the enhanced apparent expansion in vertical direction leads to a minor reduction of the small vertical stresses, while the reduced in-plane thermal expansion leads to slightly less compressive longitudinal and transverse stresses. This difference in the compressive regime leads to higher tensile stresses after cooldown which is inherited for the following re-heating cycles.

Fig. 16 shows the longitudinal, transverse, and vertical stress distributions in a longitudinal cut through the cantilever centre and a top view prior to support removal. All normal stress components predicted by the $\varepsilon_{th} + \varepsilon_{tr}$ model exceed the predictions of the ε_{th} model. The distortion after cutting is predominantly determined by the residual longitudinal stress prior to the removal of the supports. These are strongly tensile and significantly larger and more extended in the $\varepsilon_{th} + \varepsilon_{tr}$ model prediction, which explains the larger deflections upon stress relief following support removal. Furthermore, the vertical stresses are significantly smaller than the in-plane stresses which is likely due to the relatively small thickness of the cantilever. It is argued, that with increasing wall thickness, the vertical stresses would increase, leading to a stronger impact of the anisotropic transformation strain.

As the simplified multi-layer TMPS approach using a ε_{th} model yields excellent agreement with measurements in a cut cantilever, it is hypothesized that the textured PBF-LB/M microstructure developing in the rather thin cantilever may be altered by the underlying support structure significantly enough that the anisotropic apparent expansion behaviour is lost. This could be explained by the reduced heat flux through the support structure leading to higher average temperatures in the cantilever and thus reduced cooling rates and a consequently lower tendency for prior β grains to grow epitaxially over multiple layers. This needs to be further investigated in future work. Besides, it needs to be considered that the layer-wise heat input represents an oversimplification for general part geometries. In case of a small cantilever, the time to print a layer is rather short which supports this simplification. In larger parts, however, severe in-plane temperature gradients may arise that would challenge this modelling approach.

CONCLUSIONS

Following the experimental investigation of an anisotropic apparent expansion in PBF-LB/M-fabricated Ti-6Al-4V [29], an expansion model has been developed assuming isotropic thermal strains and transversally isotropic transformation strains. This model has been implemented in an UEXPAN subroutine in the commercial FE software Abaqus enabling first simulative studies on the impact of anisotropy on the residual stress and distortion evolution during the PBF-LB/M process.

The UEXPAN model was successfully applied to predict the apparent expansion in a cylinder printed at a 45° angle.

The UEXPAN model has predicted significant differences in the vertical stress components and the induced plastic strain in a single PBF-LB/M weld track with respect to model accounting for isotropic thermal expansion. These differences are argued to originate from the varied mechanical constraints imposed by the transversally isotropic expansion.

A modified multi-layer TMPS model is presented that leads to significant improvements in the prediction of distortions in a cantilever following support structure removal. The expansion model accounting for isotropic thermal strains only was shown to yield better results than the UEXPAN model, which accounts for isotropic thermal and transversally isotropic transformation strains. Besides the simplified modelling approach neglecting in-plane temperature gradients, the actual microstructure of the cantilever may differ from the cylindrical samples used for the dilatometric experiments which form the basis of the expansion model. Such differences could be justified by the support structures which reduce the heat flux away from the process zone in the cantilever leading to a reduced temperature gradient for the formation of a typical PBF-LB/M microstructure. This will be investigated in more detail in future work.

The developed UEXPAN model may further be used to simulate the impact of post-process heat-treatments or transient operating conditions on the residual stress state. In addition, it can be applied to investigate and optimise scan strategies in order to minimize residual stresses and distortion in PBF-LB/M components.

ACKNOWLEDGEMENTS

Specimens were kindly provided by Sauber Engineering within the scope of the Innosuisse project 50397.1 IP-ENG.

References

[1] M. H. FARSHIDIANFAR, A. KHAJEPOUR and A. P. GERLICH: ‘Effect of real-time cooling rate on microstructure in Laser Additive Manufacturing’, *J. Mater. Process. Technol.*, vol. 231, pp. 468-478, May 2016, doi: 10.1016/j.jmatprotec.2016.01.017.

[2] U. SCIPIONI BERTOLI, G. GUSS, S. WU, M. J. MATTHEWS and J. M. SCHOENUNG: ‘In-situ characterization of laser-powder interaction and cooling rates through high-speed imaging of powder bed fusion additive manufacturing’, *Mater. Des.*, vol. 135, pp. 385-396, Dec. 2017, doi: 10.1016/j.matdes.2017.09.044.

[3] P. A. HOOPER: ‘Melt pool temperature and cooling rates in laser powder bed fusion’, *Addit. Manuf.*, vol. 22, pp. 548-559, Aug. 2018, doi: 10.1016/j.addma.2018.05.032.

[4] A. PFAFF, S. SCHÄFFER, M. JÄCKLEIN and F. BALLE: ‘Measuring the Cooling Behavior of Melt Pools in L-PBF by Pyrometry’, *Materials*, vol. 16, no. 10, p. 3647, May 2023, doi: 10.3390/ma16103647.

[5] P. A. KOBRYN and S. L. SEMIATIN: ‘Microstructure and texture evolution during solidification processing of Ti–6Al–4V’, *J. Mater. Process. Technol.*, vol. 135, no. 2-3, pp. 330-339, Apr. 2003, doi: 10.1016/s0924-0136(02)00865-8.

[6] S. S. AL-BERMANI, M. L. BLACKMORE, W. ZHANG and I. TODD: ‘The Origin of Microstructural Diversity, Texture, and Mechanical Properties in Electron Beam Melted Ti-6Al-4V’, *Metall. Mater. Trans. A*, vol. 41, no. 13, pp. 3422-3434, Dec. 2010, doi: 10.1007/s11661-010-0397-x.

[7] L. THIJS, F. VERHAEGHE, T. CRAEGHS, J. V. HUMBEECK and J.-P. KRUTH: ‘A study of the microstructural evolution during selective laser melting of Ti–6Al–4V’, *Acta Mater.*, vol. 58, no. 9, pp. 3303-3312, May 2010, doi: 10.1016/j.actamat.2010.02.004.

[8] B. VRANCKEN, L. THIJS, J.-P. KRUTH and J. VAN HUMBEECK: ‘Heat treatment of Ti6Al4V produced by Selective Laser Melting: Microstructure and mechanical properties’, *J. Alloys Compd.*, vol. 541, pp. 177-185, Nov. 2012, doi: 10.1016/j.jallcom.2012.07.022.

[9] C. QIU, N. J. E. ADKINS and M. M. ATTALLAH: ‘Microstructure and tensile properties of selectively laser-melted and of HIPed laser-melted Ti–6Al–4V’, *Mater. Sci. Eng. A*, vol. 578, pp. 230-239, Aug. 2013, doi: 10.1016/j.msea.2013.04.099.

[10] M. SIMONELLI, Y. Y. TSE and C. TUCK: ‘On the Texture Formation of Selective Laser Melted Ti-6Al-4V’, *Metall. Mater. Trans. A*, vol. 45, no. 6, pp. 2863-2872, Jun. 2014, doi: 10.1007/s11661-014-2218-0.

[11] M. SIMONELLI, Y. Y. TSE and C. TUCK: ‘Effect of the build orientation on the mechanical properties and fracture modes of SLM Ti–6Al–4V’, *Mater. Sci. Eng. A*, vol. 616, pp. 1-11, Oct. 2014, doi: 10.1016/j.msea.2014.07.086.

[12] A. BASAK and S. DAS: ‘Epitaxy and Microstructure Evolution in Metal Additive Manufacturing’, *Annu. Rev. Mater. Res.*, vol. 46, no. 1, pp. 125-149, Jul. 2016, doi: 10.1146/annurev-matsci-070115-031728.

[13] J. LI, X. ZHOU, M. BROCHU, N. PROVATAS and Y. F. ZHAO: ‘Solidification microstructure simulation of Ti-6Al-4V in metal additive manufacturing: A review’, *Addit. Manuf.*, vol. 31, p. 100989, Jan. 2020, doi: 10.1016/j.addma.2019.100989.

[14] W. G. BURGERS: ‘On the process of transition of the cubic-body-centered modification into the hexagonal-close-packed modification of zirconium’, *Physica*, vol. 1, no. 7-12, pp. 561-586, May 1934, doi: 10.1016/s0031-8914(34)80244-3.

[15] C. CAYRON: ‘Importance of the α→β transformation in the variant selection mechanisms of thermomechanically processed titanium alloys’, *Scr. Mater.*, vol. 59, no. 5, pp. 570-573, Sep. 2008, doi: 10.1016/j.scriptamat.2008.05.013.

[16] D. BHATTACHARYYA, G. B. VISWANATHAN, R. DENKENBERGER, D. FURRER and H. L. FRASER: ‘The role of crystallographic and geometrical relationships between α and β phases in an α/β titanium alloy’, *Acta Mater.*, vol. 51, no. 16, pp. 4679-4691, Sep. 2003, doi: 10.1016/s1359-6454(03)00179-4.

[17] M. HUMBERT, L. GERMAIN, N. GEY, P. BOCHER and M. JAHAZI: ‘Study of the variant selection in sharp textured regions of bimodal IMI 834 billet’, *Mater. Sci. Eng. A*, vol. 430, no. 1-2, pp. 157-164, Aug. 2006, doi: 10.1016/j.msea.2006.05.047.

[18] ‘Microstructure control in processing nickel, titanium and other special alloys’, in *Microstructure Evolution in Metal Forming Processes*, Elsevier, 2012, pp. 337-383. doi: 10.1533/9780857096340.3.337.

[19] J. YANG, H. YU, J. YIN, M. GAO, Z. WANG and X. ZENG: ‘Formation and control of martensite in Ti-6Al-4V alloy produced by selective laser melting’, *Mater. Des.*, vol. 108, pp. 308-318, Oct. 2016, doi: 10.1016/j.matdes.2016.06.117.

[20] N. HAGHDADI, R. DEMOTT, P. L. STEPHENSON, X. Z. LIAO, S. P. RINGER and S. PRIMIG: ‘Five-parameter characterization of intervariant boundaries in additively manufactured Ti-6Al-4V’, *Mater. Des.*, vol. 196, p. 109177, Nov. 2020, doi: 10.1016/j.matdes.2020.109177.

[21] P. L. STEPHENSON, N. HAGHDADI, R. DEMOTT, X. Z. LIAO, S. P. RINGER and S. PRIMIG: ‘Effect of scanning strategy on variant selection in additively manufactured Ti-6Al-4V’, *Addit. Manuf.*, vol. 36, p. 101581, Dec. 2020, doi: 10.1016/j.addma.2020.101581.

[22] R. DEMOTT, N. HAGHDADI, Z. GANDOMKAR, X. LIAO, S. RINGER and S. PRIMIG: ‘Formation and 3D morphology of interconnected α microstructures in additively manufactured Ti-6Al-4V’, *Materialia*, vol. 20, p. 101201, Dec. 2021, doi: 10.1016/j.mtla.2021.101201.

[23] R. DeMott, N. Haghdadi, X. Liao, S. P. Ringer and S. Primig: '3D characterization of microstructural evolution and variant selection in additively manufactured Ti-6Al-4 V', *J. Mater. Sci.*, vol. 56, no. 26, pp. 14763-14782, Sep. 2021, doi: 10.1007/s10853-021-06216-2.

[24] B. Meier *et al.*: 'Influences of Surface, Heat Treatment, and Print Orientation on the Anisotropy of the Mechanical Properties and the Impact Strength of Ti 6Al 4V Processed by Laser Powder Bed Fusion', *J. Manuf. Mater. Process.*, vol. 6, no. 4, p. 87, Aug. 2022, doi: 10.3390/jmmp6040087.

[25] R. R. Pawar and V. T. Deshpande: 'The anisotropy of the thermal expansion of α-titanium', *Acta Crystallogr. Sect. A*, vol. 24, no. 2, pp. 316-317, Mar. 1968, doi: 10.1107/s0567739468000525.

[26] D. Gehring, J. A. Monroe and I. Karaman: 'Effects of composition on the mechanical properties and negative thermal expansion in martensitic TiNb alloys', *Scr. Mater.*, vol. 178, pp. 351-355, Mar. 2020, doi: 10.1016/j.scriptamat.2019.11.052.

[27] D. Gehring, Y. Ren, Z. Barghouti and I. Karaman: 'In-situ investigation of anisotropic crystalline and bulk negative thermal expansion in titanium alloys', *Acta Mater.*, vol. 210, p. 116847, May 2021, doi: 10.1016/j.actamat.2021.116847.

[28] J. A. Monroe, D. Gehring, I. Karaman, R. Arroyave, D. W. Brown and B. Clausen: 'Tailored thermal expansion alloys', *Acta Mater.*, vol. 102, pp. 333-341, Jan. 2016, doi: 10.1016/j.actamat.2015.09.012.

[29] T. Mayer, F. Friso, and R. Radis: 'Effect of Build Orientation on Thermal Expansion of LPBF Printed Ti-6Al-4V', *Metall. Mater. Trans. A*, vol. 56, no. 4, pp. 1287-1309, Apr. 2025, doi: 10.1007/s11661-025-07706-7.

[30] J. W. Elmer, T. A. Palmer, S. S. Babu and E. D. Specht: 'In situ observations of lattice expansion and transformation rates of α and β phases in Ti–6Al–4V', *Mater. Sci. Eng. A*, vol. 391, no. 1-2, pp. 104–113, Jan. 2005, doi: 10.1016/j.msea.2004.08.084.

[31] P. P. Dhekne, M. Bönisch, M. Seefeldt and K. Vanmeensel: 'In-situ synchrotron X-ray diffraction investigation of martensite decomposition in Laser Powder Bed Fusion (L-PBF) processed Ti–6Al–4V', *Mater. Sci. Eng. A*, vol. 899, p. 146421, May 2024, doi: 10.1016/j.msea.2024.146421.

[32] P. Mercelis and J. Kruth: 'Residual stresses in selective laser sintering and selective laser melting', *Rapid Prototyp. J.*, vol. 12, no. 5, pp. 254-265, Oct. 2006, doi: 10.1108/13552540610707013.

[33] M. Matsumoto, M. Shiomi, K. Osakada and F. Abe: 'Finite element analysis of single layer forming on metallic powder bed in rapid prototyping by selective laser processing', *Int. J. Mach. Tools Manuf.*, vol. 42, no. 1, pp. 61-67, Jan. 2002, doi: 10.1016/s0890-6955(01)00093-1.

[34] I. A. Roberts, C. J. Wang, R. Esterlein, M. Stanford and D. J. Mynors: 'A three-dimensional finite element analysis of the temperature field during laser melting of metal powders in additive layer manufacturing', *Int. J. Mach. Tools Manuf.*, vol. 49, no. 12-13, pp. 916-923, Oct. 2009, doi: 10.1016/j.ijmachtools.2009.07.004.

[35] M. F. Zaeh and G. Branner: 'Investigations on residual stresses and deformations in selective laser melting', *Prod. Eng.*, vol. 4, no. 1, pp. 35-45, Feb. 2010, doi: 10.1007/s11740-009-0192-y.

[36] N. Contuzzi, S. L. Campanelli and A. D. Ludovico: '3D Finite Element Analysis in the selective laser melting process', *Int. J. Simul. Model.*, vol. 10, no. 3, pp. 113-121, Sep. 2011, doi: 10.2507/ijsimm10(3)1.169.

[37] A. HUSSEIN, L. HAO, C. YAN and R. EVERSON: ‘Finite element simulation of the temperature and stress fields in single layers built without-support in selective laser melting’, *Mater. Des. 1980-2015*, vol. 52, pp. 638-647, Dec. 2013, doi: 10.1016/j.matdes.2013.05.070.

[38] W. KING, A. T. ANDERSON, R. M. FERENCZ, N. E. HODGE, C. KAMATH and S. A. KHAIRALLAH: ‘Overview of modelling and simulation of metal powder bed fusion process at Lawrence Livermore National Laboratory’, *Mater. Sci. Technol.*, vol. 31, no. 8, pp. 957–968, Jun. 2015, doi: 10.1179/1743284714y.0000000728.

[39] L. PARRY, I. A. ASHCROFT and R. D. WILDMAN: ‘Understanding the effect of laser scan strategy on residual stress in selective laser melting through thermo-mechanical simulation’, *Addit. Manuf.*, vol. 12, pp. 1-15, Oct. 2016, doi: 10.1016/j.addma.2016.05.014.

[40] J. WU, L. WANG and X. AN: ‘Numerical analysis of residual stress evolution of AlSi10Mg manufactured by selective laser melting’, *Optik*, vol. 137, pp. 65-78, May 2017, doi: 10.1016/j.ijleo.2017.02.060.

[41] P. CONTI, F. CIANETTI and P. PILERCI: ‘Parametric Finite Elements Model of SLM Additive Manufacturing process’, *Procedia Struct. Integr.*, vol. 8, pp. 410-421, 2018, doi: 10.1016/j.prostr.2017.12.041.

[42] Z. DONG, Y. LIU, W. WEN, J. GE and J. LIANG: ‘Effect of Hatch Spacing on Melt Pool and As-built Quality During Selective Laser Melting of Stainless Steel: Modeling and Experimental Approaches’, *Materials*, vol. 12, no. 1, p. 50, Dec. 2018, doi: 10.3390/ma12010050.

[43] Q. ZHANG, J. XIE, Z. GAO, T. LONDON, D. GRIFFITHS and V. OANCEA: ‘A metallurgical phase transformation framework applied to SLM additive manufacturing processes’, *Mater. Des.*, vol. 166, p. 107618, Mar. 2019, doi: 10.1016/j.matdes.2019.107618.

[44] Q. ZHANG, J. XIE, T. LONDON, D. GRIFFITHS, I. BHAMJI and V. OANCEA: ‘Estimates of the mechanical properties of laser powder bed fusion Ti-6Al-4V parts using finite element models’, *Mater. Des.*, vol. 169, p. 107678, May 2019, doi: 10.1016/j.matdes.2019.107678.

[45] N. E. HODGE, R. M. FERENCZ and J. M. SOLBERG: ‘Implementation of a thermomechanical model for the simulation of selective laser melting’, *Comput. Mech.*, vol. 54, no. 1, pp. 33-51, Jul. 2014, doi: 10.1007/s00466-014-1024-2.

[46] N. E. HODGE, R. M. FERENCZ and R. M. VIGNES: ‘Experimental comparison of residual stresses for a thermomechanical model for the simulation of selective laser melting’, *Addit. Manuf.*, vol. 12, pp. 159-168, Oct. 2016, doi: 10.1016/j.addma.2016.05.011.

[47] C. LI, J. F. LIU and Y. B. GUO: ‘Prediction of Residual Stress and Part Distortion in Selective Laser Melting’, *Procedia CIRP*, vol. 45, pp. 171-174, 2016, doi: 10.1016/j.procir.2016.02.058.

[48] C. LI, J. F. LIU, X. Y. FANG and Y. B. GUO: ‘Efficient predictive model of part distortion and residual stress in selective laser melting’, *Addit. Manuf.*, vol. 17, pp. 157-168, Oct. 2017, doi: 10.1016/j.addma.2017.08.014.

[49] Y. YANG, M. ALLEN, T. LONDON and V. OANCEA: ‘Residual Strain Predictions for a Powder Bed Fusion Inconel 625 Single Cantilever Part’, *Integrating Mater. Manuf. Innov.*, vol. 8, no. 3, pp. 294-304, Sep. 2019, doi: 10.1007/s40192-019-00144-5.

[50] X. SONG *et al.*: ‘Advances in additive manufacturing process simulation: Residual stresses and distortion predictions in complex metallic components’, *Mater. Des.*, vol. 193, p. 108779, Aug. 2020, doi: 10.1016/j.matdes.2020.108779.

[51] J. GOLDAK, A. CHAKRAVARTI and M. BIBBY: ‘A new finite element model for welding heat sources’, *Metall. Trans. B*, vol. 15, no. 2, pp. 299-305, Jun. 1984, doi: 10.1007/BF02667333.

[52] A. J. Dunbar, E. R. Denlinger, M. F. Gouge and P. Michaleris: ‘Experimental validation of finite element modeling for laser powder bed fusion deformation’, *Addit. Manuf.*, vol. 12, pp. 108-120, Oct. 2016, doi: 10.1016/j.addma.2016.08.003.

[53] N. Keller and V. Ploshikhin: ‘New method for fast predictions of residual stress and distortion of AM parts’, in *Additive Manufacturing Conference SFF 2014*, 2014, pp. 1229-1237.

[54] X. Liang, Q. Chen, L. Cheng, D. Hayduke and A. C. To: ‘Modified inherent strain method for efficient prediction of residual deformation in direct metal laser sintered components’, *Comput. Mech.*, vol. 64, no. 6, pp. 1719-1733, Dec. 2019, doi: 10.1007/s00466-019-01748-6.

[55] M. Chiumenti *et al.*: ‘Numerical modelling and experimental validation in Selective Laser Melting’, *Addit. Manuf.*, vol. 18, pp. 171-185, Dec. 2017, doi: 10.1016/j.addma.2017.09.002.

[56] L. Levine *et al.*: ‘Outcomes and Conclusions from the 2018 AM-Bench Measurements, Challenge Problems, Modeling Submissions, and Conference’, *Integrating Mater. Manuf. Innov.*, vol. 9, no. 1, pp. 1-15, Mar. 2020, doi: 10.1007/s40192-019-00164-1.

[57] Ansys: ‘Ansys Additive Manufacturing 2024 R2 - LPBF Simulation Guide’, ANSYS Inc. Accessed: Jul. 21, 2025, [Online], Available: https://ansyshelp.ansys.com/public/account/secured?returnurl=//////Views/Secured/corp/v242/en/add_ag/add_ag.html

[58] T. Mayer, G. Brändle, A. Schönenberger and R. Eberlein: ‘Simulation and validation of residual deformations in additive manufacturing of metal parts’, *Heliyon*, vol. 6, no. 5, p. e03987, May 2020, doi: 10.1016/j.heliyon.2020.e03987.

[59] R. Enos: ‘Install Abaqus 2024 User-Subroutines: How to Link Abaqus 2024 with Intel oneAPI Fortran Compiler & Visual Studio’, Feb. 2024, [Online], Available: DOI: 10.13140/RG.2.2.15382.11843

[60] Dassault Systemes: ‘SIMULIA Abaqus - User Subroutines - Abaqus/Standard User Subroutines - UEXPAN’, [Online], Available: https://docs.software.vt.edu/abaqusv2023/English/?show=SIMACAESUBRefMap/simasub-c-uexpan.htm

[61] E. Mirkoohi, D. E. Seivers, H. Garmestani and S. Y. Liang: ‘Heat Source Modeling in Selective Laser Melting’, *Materials*, vol. 12, no. 13, p. 2052, Jun. 2019, doi: 10.3390/ma12132052.

[62] S. Hocine, H. Van Swygenhoven and S. Van Petegem: ‘Verification of selective laser melting heat source models with operando X-ray diffraction data’, *Addit. Manuf.*, vol. 37, p. 101747, Jan. 2021, doi: 10.1016/j.addma.2020.101747.

[63] M. Liu *et al.*: ‘A characteristic time-based heat input model for simulating selective laser melting’, *Addit. Manuf.*, vol. 44, p. 102026, Aug. 2021, doi: 10.1016/j.addma.2021.102026.

[64] ‘Ti: Ti-6 Al-4 V (IMI 318)’, in *Recommended Values of Thermophysical Properties for Selected Commercial Alloys*, Elsevier, 2002, pp. 211–217. doi: 10.1533/9781845690144.211.

[65] G. Welsch, R. Boyer and E. W. Collings: Eds., *Materials properties handbook: titanium alloys*. Materials Park, OH: ASM International, 1994.

[66] Dassault Systemes: ‘SIMULIA Abaqus - Materials - Other Material Properties - Mechanical Properties - Thermal Expansion’. [Online]. Available: https://docs.software.vt.edu/abaqusv2023/English/?show=SIMACAEMATRefMap/simamat-c-thermalexpan.htm.